Molecular modeling of the time-dependent shock response in polyurea with Hugoniostat and explicit impact simulations

Benjamin Xu [*] and Thomas C. O'Connor [†]
Department of Materials Science and Engineering, Carnegie Mellon University, Pittsburgh, Pennsylvania 15213, USA

(Received 15 December 2025; revised 19 April 2026; accepted 12 May 2026; published 25 June 2026)

Molecular dynamics simulations are applied to study the shock response of the hard and soft phases of nanostructured polyureas. Shocks are modeled using both a nonequilibrium explicit impact method and a quasistatic Hugoniostat method. These methods subject systems to different strain rate histories, resulting in dissimilarities in the transient evolution of the thermodynamic state of the material during shock loading. Once materials are compressed into glassy states, both Hugoniostat and impact simulations display similar Eyring-like relaxation of the residual shear stress corresponding to a logarithmic slowdown in plastic deformation post-shock. The slowly relaxing shear stress makes the prediction of post-shock densities and shock speeds sensitive to total simulation time. While Hugoniostats can efficiently resolve the steady-state limiting Hugoniot, our results indicate that this is unlikely to be realized in experiments over the timescales during which shocks transit real microstructures. Instead, real shocks will travel at transient shock speeds governed by the dynamic stress relaxation of the relevant phases, which can be predicted by explicit impact simulations.

DOI: 10.1103/p577-s387

I. INTRODUCTION

Polyurea is an elastomer valued for its high mechanical toughness, chemical resistance, and energy dissipation [1–3]. These qualities have popularized its usage as a lightweight protective spray coating for applications necessitating impact and blast mitigation, including structures [1,2], personal protective equipment [4], and dampers for automotive and aerospace vehicles [5]. In the recent literature, there has been increased interest in the study of polyurea for attenuating shock waves [6–18], supersonic disturbances that adiabatically drive materials to nonequilibrium thermodynamic states as they propagate. Despite widespread commercial use of polyurea, the molecular mechanisms controlling its high-rate mechanical behavior are not fully understood. Bespoke structural tailoring of polyurea for relevant applications, together with the synthesis of other nanostructured polymers for the purposes of impact mitigation, requires an improved understanding of how the morphology of polyurea contributes toward shock dissipation.

Characterization of polymer microstructures during shock impact is difficult due to the inherently short time and length scales associated with experiments. As a result, computational modeling and simulation methods, such as molecular dynamics (MD), have been relied upon to provide a molecular-level interpretation of the mechanics of soft materials under shock [19–24].

Methodologies for shock simulation typically belong to one of two groups. The first, which we refer to as *explicit impact methods*, simulates a piston striking a sample to produce a propagating shock wave [25–29], similar to plate impact experiments. These methods are computationally expensive because they require long simulation boxes to resolve and measure the steady fronts of rapidly propagating shock fronts. They are also limited in their total time evolution since they must end once the transiting front crosses the simulation cell.

The second set of methods, which we refer to as *equilibrium methods*, do not model impact explicitly. Rather, they aim to simulate material in the steady post-shock state for a specific impact strength. This is done by using the Rankine-Hugoniot conservation relations to control the pressure and temperature of the material. These methods, such as the multiscale shock technique (MSST) [30] and the uniaxial constant-volume [31] or constant-stress Hugoniostats [32], can be used to measure the shock Hugoniots of materials using much smaller system sizes and enable simulations to reach much longer timescales [32].

Several multiscale MD simulations have been conducted using explicit and equilibrium impact methods to investigate the shock response of polyurea, citing the mechanics, composition, and chain architecture of its nanoscale morphology as key factors governing its dynamics [9–11,14–18]. Despite recent progress, accurately capturing the impact of the phase-segregated morphology of polyurea during shock loading remains a nontrivial task. Atomistic-scale models can capture local representations of the morphology [9,10], but struggle to model larger-scale bulk microstructures due to the prohibitively slow kinetics of molecular self-assembly. Conversely, coarse-grained representations have been used to model microphase separation at mesoscopic time and length scales [3,11,13,14,33–35], but forgo the ability to explore the influence of atomistic mechanisms such as hydrogen bonding and π–π stacking.

[*]Contact author: benjamix@andrew.cmu.edu
[†]Contact author: thomaso@andrew.cmu.edu

An alternative approach to characterizing the shock response of multiphase materials is through the use of mixture models [36–46]. Early methods made predictions for the equations of state of simple mixtures by interpolating their pressure-volume Hugoniots at constant pressures based on the volume fraction of each component, finding fair agreement with experimental data for semicrystalline polyethylene and binary metal composites and alloys [36,38]. More recently, Jordan *et al.* [45] have developed a mixture model capable of predicting shock equations of state for multi-component composites with varying material classes such as metallic alloys and polymer matrix composites. Their predictions fall within an accuracy of the experimental data similar to that of mesoscale models, bypassing the need to directly prepare and characterize high-fidelity microstructures. To reduce the propagation of errors, these models require precise measurements of the shock equations of state of the constituent phases and an improved understanding of how the properties of individual phases influence those of the bulk composite.

A recent MD study by Manav *et al.* [15] validated the use of mixture models to predict the shock Hugoniot of polyurea. The authors created representative volume elements to separately model the mechanically dissimilar constituents within the nanophase-segregated morphology of polyurea. This enabled them to individually characterize the bulk solid mechanics of the glassy and rubbery component phases. Using different composition-based mixing rules [38,47], they were able to compute equations of state for polyurea under quasistatic uniaxial compression and high-rate shock impact that were in good agreement with those of experiments [12,15].

Using equilibrium shock simulations, Manav *et al.* [15] were also able to measure an increasing disruption of aromatic carbon arrangements and hydrogen bonds in the glassy phase with stronger shocks, indicating significant shock induced plasticity. Given the inherent strain rate sensitivity of polyurea [48] and the artificial loading conditions imposed by equilibrium shock simulations, it is unclear whether these plastic rearrangements are comparable to those produced by propagating shock waves in explicit impact simulations. Previous studies have reported good agreement for the shock equations of state predicted by equilibrium and impact methods [30–32,49,50]. However, recent work by Lecoutre *et al.* [49] found that their equilibrium shock simulations induced only a static residual shear stress representative of purely elastic deformation rather than a transient deviatoric stress relaxation typically produced by plastic shocks.

In this study, we leverage the models of Manav *et al.* [15] to investigate the shock induced plastic deformation of two linear homopolymers with distinct chemistries. We create atomic-scale representative volume elements of the "hard" glassy and "soft" rubbery nanodomains within polyurea and verify that our models reproduce the equilibrium Hugoniot shocks of previous studies [15]. Comparing equilibrium and explicit impact shocks, we find that both methods induce a similar time-dependent shear stress relaxation in the hard and soft phases. The stress relaxation curves of both phases are fit to a single-barrier stress-activated Eyring model, suggesting that both hard and soft phases exhibit similar glassy mechanics under shock compression despite showing glassy and rubbery behavior under ambient conditions, respectively.

TABLE I. OPLS interactions and functional forms.

Interaction type	Functional form
Bond	$E = K_b(r - r_0)^2$
Angle	$E = K_\theta(\theta - \theta_0)^2$
Dihedral	$E = \frac{1}{2}K_1[1 + \cos(\phi)] + \frac{1}{2}K_2[1 - \cos(2\phi)]$ $+\frac{1}{2}K_3[1 + \cos(3\phi)] + \frac{1}{2}K_4[1 - \cos(4\phi)]$
Improper	$E = K_I[1 + d\cos(n\phi)]$
Non-bonded	$E = 4\epsilon[(\sigma/r)^{12} - (\sigma/r)^6]$ $r < r_c$
Electrostatic	$E = Cq_iq_j/\epsilon r$ $r < r_c$

This logarithmically slow plasticity corresponds to the gradual densification of our models, which is resolved on significantly longer timescales than those of shock propagation within the nanoscale microstructure of polyurea. This results in noticeably larger shock velocities measured during impacts compared to those from equilibrium shock simulations.

II. METHODS

A. Atomic potential and integration

Polyurea is modeled using the OPLS-AA (Optimized Potentials for Liquid Simulations – All Atom) force field [51]. Past studies using this force field have validated the stress-strain relation of polyurea with experiments under uniaxial compression up to pressures of approximately 10 GPa [12]. Reactivity and rearrangement of chemical bonds are typically not prevalent within polyurea for shocks of this magnitude [52] and, thus, are not considered in our simulations.

The functional forms for the bonded and non-bonded interactions for the force field are given in Table I. Bonded interactions are made up of bond stretching, angle, and dihedral energy terms. Non-bonded interactions are modeled with a Lennard-Jones (LJ) potential and a Coulomb potential. For non-bonded interactions between atoms less than 4 bonds apart, 1-2 and 1-3 interactions are excluded, while 1-4 interactions are weighted by a factor of 0.5. LJ interactions are truncated at a cutoff distance $r_c = 10$ Å. Long-range Coulomb interactions are computed using a particle-particle/particle-mesh (PPPM) scheme [53] with an equivalent short range cutoff of r_c. We use a k-space grid spacing of 3.825 Å for all systems, which results in a relative RMS error in the electrostatic force of 10^{-4} per-atom. Atoms are parameterized for OPLS-AA using LigParGen and the 1.14*CM1A charge model [54–56], with the parametrization of different atom types listed in Ref. [57].

Molecular dynamics (MD) simulations are performed using the LAMMPS simulation code [58]. A velocity-Verlet integrator with a timestep of 1 fs is used for equilibration and equilibrium shock simulations, while a shorter timestep of 0.1 fs is used for explicit impact simulations to ensure stability. Initial equilibration of small samples used in equilibrium simulations is conducted in the NPT ensemble using a Nosé-Hoover thermostat and barostat with time damping parameters equal to 100 and 1000 fs, respectively. Explicit impacts are performed in the NVE ensemble to model adiabatic shock conditions similar to those of experiments. Systems have periodic boundary conditions that span all three axes.

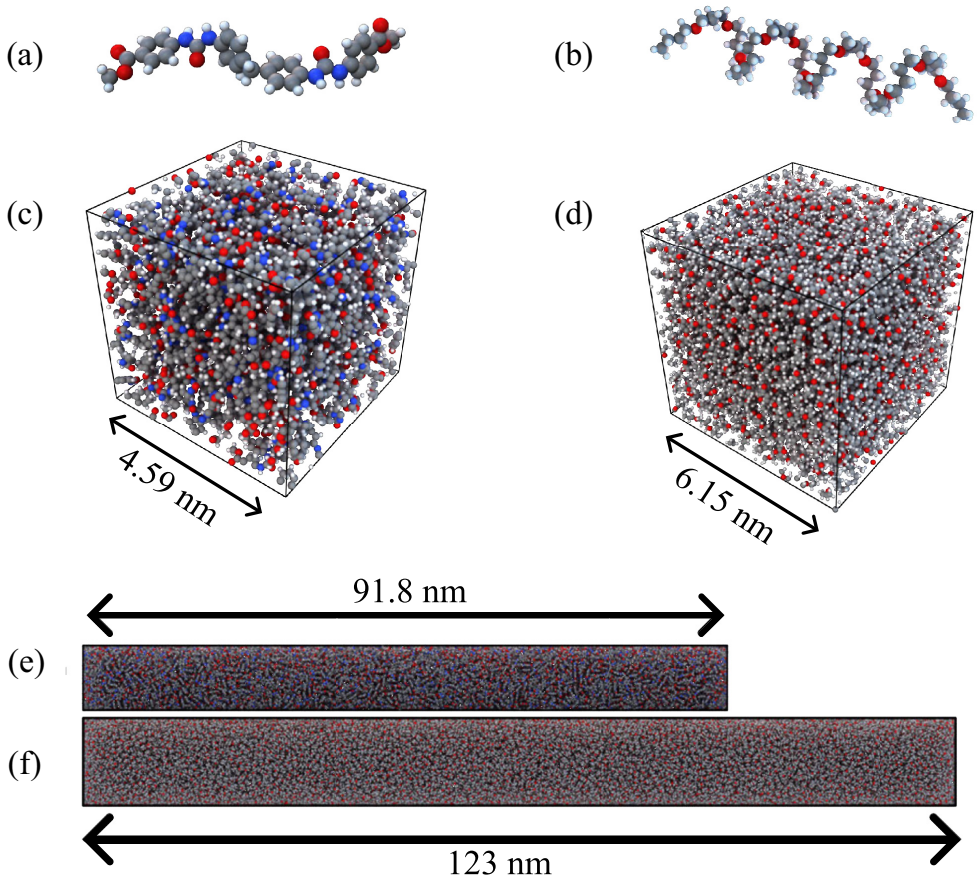

FIG. 1. Molecular structures used to model the composition of hard (a) and soft (b) phases within nanophase separated polyurea. Grey, red, blue, and white beads represent carbon, oxygen, nitrogen, and hydrogen atoms, respectively. Representative bulk hard (c)/soft (d) phase systems composed of 125 hard/soft molecules equilibrated at ambient conditions. Longer systems for explicit impact simulations (e) and (f) were constructed by replicating (c) and (d) 20-fold along the x axis.

B. Model chemistry and preparation

Polyurea 1000 is the target polymer chemistry that we intend to model for this study. This block copolymer is synthesized through bulk polymerization of 80 wt% of an oligomeric amine and 20 wt% of a multifunctional isocyanate curative [6]. A typical commercial variant uses poly(tetramethylene oxide) di-p-aminobenzoate ($n = 14$) (Versalink P-1000, Evonik) and auritoneimine-modified diphenylmethane diisocyanate (Isonate 143L, Dow) as components. Due to the proprietary nature of Isonate 143L, which includes an undisclosed combination of difunctional and trifunctional isocyanates among other additives, prior modeling studies have assumed the use of difunctional 4,4'-methylene bis(phenyl isocyanate) (MDI) as an alternative isocyanate [3,12,15]. Given that the average functionality of Isonate 143L is relatively similar at 2.1 [59], these models have shown good agreement of viscoelastic and high-rate mechanical behavior with experiments.

Chains in molten polyurea self-assemble as the urea-rich segments segregate to form hydrogen bonds and undergo π-π stacking [14,59]. This results in the formation of microphase separated nanostructures consisting of "hard" domains interspersed in a "soft" matrix. Under ambient conditions, the hard phase is below its glass transition temperature (T_g) and possesses the mechanical response of a brittle glass, while the soft phase is slightly above its T_g and exhibits rubber-like behavior. We create representative volume elements of the hard and soft phases using a strategy similar to that of Manav *et al.* [15]. The block copolymer chemistry of polyurea is first spliced into two separate components for populating our bulk models. The representative hard molecule, shown in Fig. 1(a), is effectively a diphenyl-methane diisocyanate end-functionalized with two methyl 4-aminobenzoates. This arrangement suppresses artificial hydrogen bond formation caused by ending the hard domain molecule at an oxygen atom [15]. The soft molecule, shown in Fig. 1(b), is composed of the remainder of the poly(tetramethylene oxide) di-p-aminobenzoate molecule, resulting in a repeating chain of four carbons and one oxygen atom.

To create initial configurations, both hard and soft molecules are replicated 125 times within separate simulation boxes. These systems are annealed at a pressure of 1 atm and temperatures of 800 and 500 K for the hard and soft phases, respectively, which are above the individual glass transition temperatures of each composition [15]. Annealing is conducted long enough so that the molecules can diffuse several times their size and randomize their initial configurations. The systems are then quenched at a rate of 25 K/ns down to 300 K, resulting in amorphous microstructures. The systems are equilibrated at 300 K and 1 atm for 10 ns, achieving equilibrium densities of $\rho_{\text{hard}} = 1.2004$ g/cm^3 and $\rho_{\text{soft}} = 0.9352$ g/cm^3.

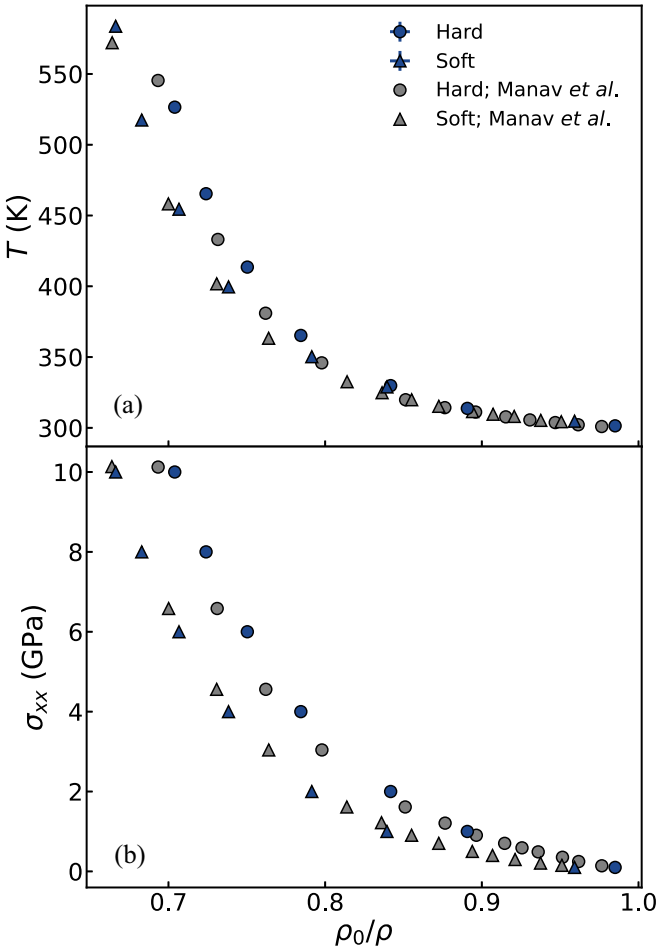

FIG. 2. (a) Temperature T and (b) normal stress σ_{xx} vs relative density ρ_0/ρ Hugoniots for hard and soft phases compared with those from Manav *et al.* [15].

The cubic simulation box lengths were 4.57 and 6.19 nm for the hard and soft models, respectively, as visualized in Figs. 1(c) and 1(d).

For explicit impact simulations, larger simulation cells are required to resolve and measure propagating shock waves. For sample preparation, we switch to the NVT ensemble to prepare for the constant volume conditions present during impact simulations. Equilibrated models at 300 K are first isotropically deformed to their equilibrium densities. Systems are then replicated 20-fold along the x axis to create the longer systems (91.8/123 nm for the hard/soft phase) visualized in Figs. 1(e) and 1(f). System sizes were chosen to enable the measurement of shocks across time and length scales on the order of those of shocks propagating through realistic polyurea nanostructures [59]. The configurations are annealed again at 800 and 500 K for the hard and soft phases, respectively, and subsequently quenched to 300 K at 25 K/ns. This is followed by a brief equilibration to thermalize the systems at 300 K prior to simulating impact.

C. Hugoniostat shock methodology

To perform equilibrium shock simulations, we use the uniaxial constant-stress Hugoniostat method of Ravelo *et al.* [32].

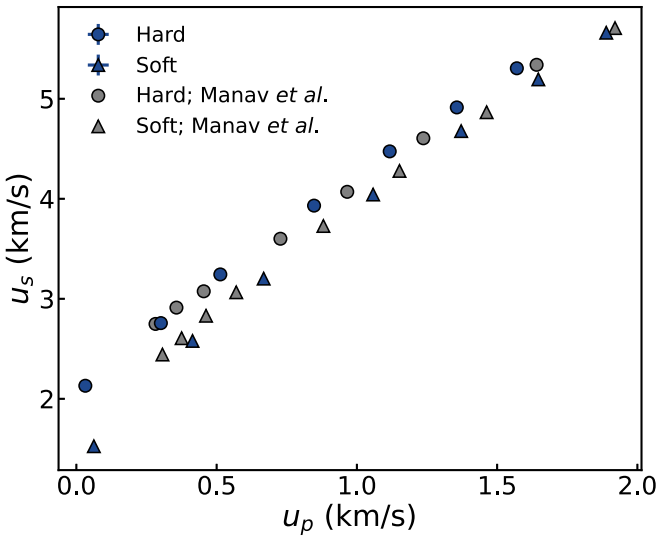

FIG. 3. Shock velocity u_s vs particle velocity u_p Hugoniots for hard and soft phases compared with those from Manav *et al.* [15].

A barostat applies a uniaxial strain compression to the system to establish a specified normal stress σ_{xx}, while an ergostat regulates the internal energy of the system to satisfy the Rankine-Hugoniot jump conditions. The barostat and ergostat operate on user-specified timescales that must be tuned to enable the evolution of the stress tensor and temperature in a manner similar to the evolution imposed by a transiting shock front. Our choices of barostat and ergostat frequencies vary by system and shock intensity to induce an appropriate strain rate. Our methodology follows the prescription of Ravelo *et al.* [32] and system specific parameters are provided in Ref. [57].

Target normal stresses σ_{xx} for the Hugoniostat are chosen within the range of 0.01 to 10 GPa, far below the values expected to lead to bond scission [52]. The Hugoniotstat also requires specifying a quiescent state (P_0, ρ_0, E_0), which we take to be the equilibrium thermodynamic state of the system at $T = 300$ K and $P = 1$ atm. Simulations at each target stress are run for 20 ns, a sufficiently long time for thermodynamic quantities to reach steady values. Statistics from the final 5 ns of the simulation were used to evaluate the Hugoniot state for each shock pressure.

To verify the shock response of our models during Hugoniostat shocks, we compare our results with those published by Manav *et al.* [15]. Figures 2 and 3 plot the shock Hugoniots of our hard and soft phases with those of Manav *et al.* [15]. The comparison yields strong agreement between the curves for both hard and soft phases. In Fig. 2, we plot the temperature and normal stress as a function of relative density for both phases. The quiescent states of both systems lie at the rightmost point where $T_0 = 300$ K and $\sigma_{xx,0} = 1$ atm. Compressive shocks cause the material to densify, raising the temperature and stress of the material in a nonlinear manner. The stiffness of the "hard" phase relative to the "soft" phase is apparent given its faster rise in stress under compression.

In Fig. 3, we plot the shock velocity u_s versus the particle velocity u_p for both phases. Given the lack of a physically propagating shock wave in Hugoniostat simulations, these

values are extracted using the following Rankine-Hugoniot relations:

$$u_s = v_0\sqrt{\frac{\sigma_{xx} - P_0}{v_0 - v}}, \tag{1}$$

$$u_p = \sqrt{(\sigma_{xx} - P_0)(v_0 - v)}, \tag{2}$$

where v_0 and v are the pre- and post-shock specific volumes of our system. u_s increases linearly with increasing u_p in both phases with curves deviating from linearity for weaker shocks, as expected for shocks of this magnitude within polyurea [6,7]. The higher stiffness of the hard phase under shock is reflected in the higher shock speeds u_s in the hard phase relative to the soft phase at the same u_p.

D. Shock impact methodology and analysis techniques

Explicit impact simulations are performed using an approach similar to that of O'Connor *et al.* [22], where a rigid slab of atoms acts as a piston and impacts the material. Other methods for simulating shock impacts have been used in the literature [25–29], but He *et al.* have shown that barring material very close to the piston, these techniques produce the same shock behavior [20]. After equilibration, atoms within 1 nm of the simulation box boundaries along the x axis are constrained to act as rigid slabs, with their interactions, forces, and velocities removed. The left slab is prescribed to compress the material at a constant velocity u_p, while the right slab is fixed, generating a propagating shock front through the material. We vary u_p between 0.25–1.75 km/s, covering the range of typical flyer plate experiments.

To monitor the evolving thermodynamic state during shock propagation, we subdivide the system along the propagation axis into bins of width $\Delta x = 1$ nm and compute thermodynamic quantities averaged across all atoms within each subsystem. The local stress tensor of each bin is computed, including both thermal and virial contributions. The equation used by LAMMPS is

$$\begin{aligned}\sigma_{ij} = -\frac{1}{V_{\text{bin}}}\sum_{\alpha}^{N_{\text{bin}}}\Bigg[& mu_i u_j + \frac{1}{2}\sum^{\text{pairs}}(r_{i,1}f_{j,1} + r_{i,2}f_{j,2}) \\ & + \frac{1}{3}\sum^{\text{triples}}(r_{i,1}f_{j,1} + r_{i,2}f_{j,2} + r_{i,3}f_{j,3}) \\ & + \frac{1}{4}\sum^{\text{quads}}(r_{i,1}f_{j,1} + r_{i,2}f_{j,2} + r_{i,3}f_{j,3} + r_{i,4}f_{j,4}) \\ & + \text{Kspace}(r_i, f_j)\Bigg]_{\alpha},\end{aligned} \tag{3}$$

where V_{bin} is the volume of the bin, α indexes the atom within a bin, u is the velocity of the atom, and f_j is the force on the atom α along j. Stresses and other thermodynamic variables are calculated every 0.1 ps.

The $t - x$ plot in Fig. 4 shows an example of the normal stress $\sigma_{xx}(x, t)$ as a shock propagates through a hard-phase sample. The color indicates the local stress at each position and time. The interface between the leftmost black and purple regions is where the piston contacts the material and travels at a constant speed $u_p = 1$ km/s. The boundary between the purple and rightward black regions is the location of the shock front propagating at a velocity u_s into quiescent material. As it travels, it raises the normal stress σ_{xx} from 1 atm under ambient conditions to ≈5 GPa behind the front. After the shock front strikes the stationary right-end slab, it reflects and propagates back into the material before being reflected again off the piston as indicated by the boundaries between the purple and pink regions and pink and yellow regions, respectively. We do not analyze data after the initial reflection at the opposing end of the system. A corresponding visualization of the system at $t = 5$ ps indicated by the dotted red line is shown above the main plot, where the yellow and purple regions represent the shocked and quiescent material, respectively.

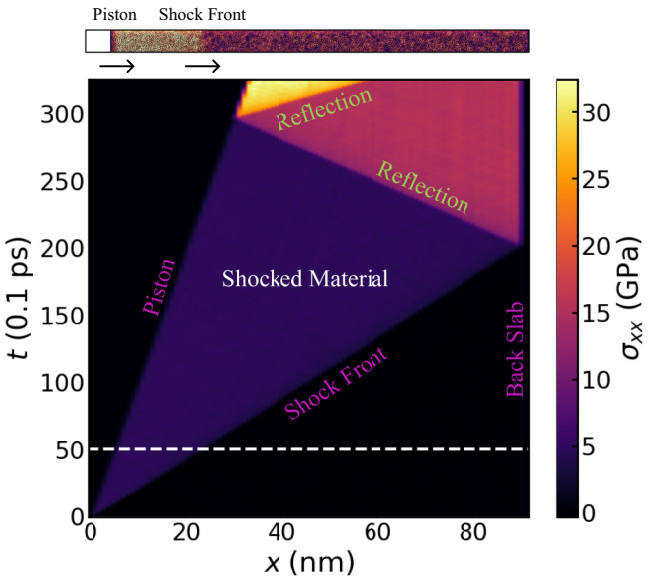

FIG. 4. Position-time ($x - t$) diagram of normal stress σ_{xx} for a 20x1x1 replicated hard phase system with $u_p = 1$ km/s. The dashed white line corresponds to the atomic configuration above the plot at $t = 5$ ps, where the piston and shock front travel towards the right. Atoms are colored by their coordination.

u_s is measured by tracking the position of the shock front over time. A Savitzky-Golay filter is used to smooth out and numerically compute the first derivative of the binned $u_p(x)$ data in the material at each time frame. The front position is determined as the maximum in the first derivative and u_s was determined using a linear least-squares fit of the front position versus time.

To compute the shock Hugoniots for direct shock simulations, we evaluate the thermodynamic state of the material behind the shock front for each u_p. Figure 5 plots the temperature T and normal stress σ_{xx} profiles of the hard (left) and soft (right) phase materials for increasing distance behind the shock front x_{BF} for each u_p. Material within 15 nm of the piston is omitted from the analysis since its proximity to the rigid piston causes it to deviate from the bulk response [20]. The stress evolution slows around $x_{BF} \approx 15$ nm behind the front in both phases. Both density ρ and particle velocity u_p also reach somewhat steady values over this distance. However, the temperature continues to exhibit a gradual increase beyond the shock front, indicating continued heating in the material after

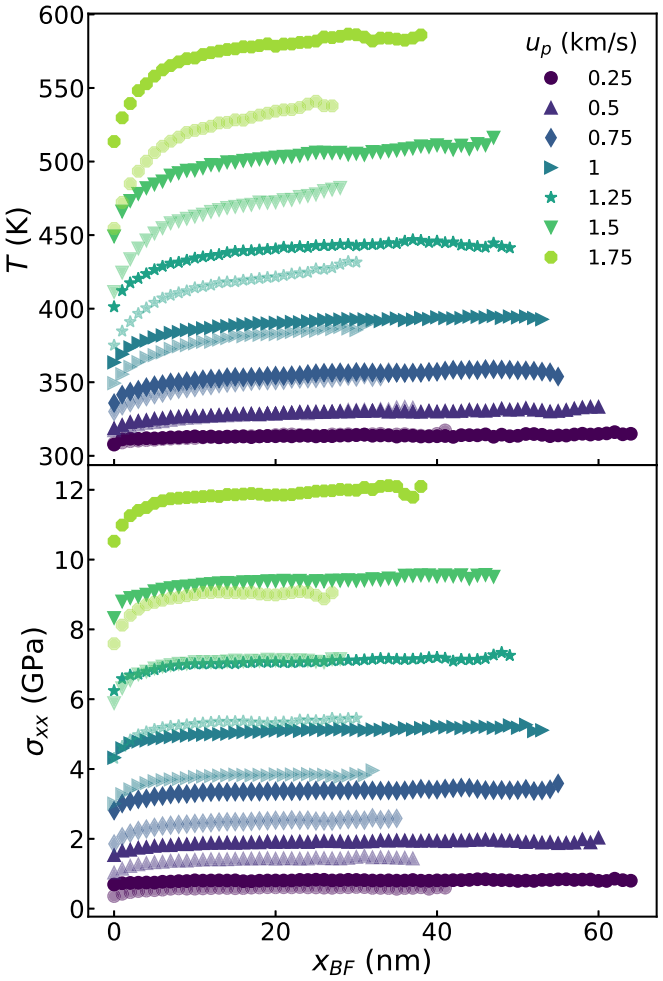

FIG. 5. Temperature T and normal stress σ_{xx} of shocked hard (opaque symbols) and soft (translucent symbols) phase material at increasing distance behind the shock front x_{BF} for all u_p.

the initial rise at the front. From these profiles, we measure the post-shock state by averaging over material in the range $x_{BF} \in [20, 30]$ nm for the hard phase and $x_{BF} \in [15, 25]$ nm for the soft phase.

III. RESULTS AND DISCUSSION

A. Strain rates

Given that polyurea is known to display a rate-sensitive mechanical response [48], it is worthwhile to compare the strain rate histories imposed by the Hugoniostat and explicit impact methods. This also allows us to verify that we have calibrated the Hugoniostat time constants to produce loading rates consistent with impact simulations.

For explicit impacts, we compute the strain rates imposed by the shock front by fitting a cubic spline to the engineering strain curve $\epsilon_{xx}(t)$ and taking a numerical derivative with respect to time. Figure 6 plots both the strain [(a) and (b)] and the corresponding strain rate profiles [(c) and (d)] as a function of time. The strain follows a sigmoidal shape that can be described by an amplitude ϵ and a rise time t_r. This is related to the width of the shock front $\lambda \sim t_r u_s$. Stronger shocks induce larger strains and propagate at faster u_s, leading to shorter rise times and higher strain rates [60]. The sigmoidal strain profile results in a peaked strain rate history with a peak rate that scales as $\sim\epsilon/t_r$. Away from the front, the strain rate gradually decreases back towards zero as the material tends toward steady state.

Hugoniostat simulations vary the length L_x of the x axis of the simulation cell to simulate shock loading. Thus, we compute an engineering strain rate via $\dot{\epsilon}_{xx} = (dL_x/dt)/L_x(0)$, computing the time derivative using a Savitsky-Golay filter. Figure 7 plots the strain rate during the first 1.25 ps of Hugoniostat shock simulations for all shocks. For both phases, the systems exhibit an overdamped decay in the strain rate. The transient strain rate of Hugoniostat simulations is controlled by our choice of barostat and ergostat parameters, which we vary for each prescribed normal stress σ_{xx} via the methodology prescribed by Ravelo *et al.* [32] (see Ref. [57]). This process should give strain rates of a similar magnitude to impact simulations of similar shock strength. This is true for the maximum strain rates for soft phases, with both methods producing rates ranging between $\sim 10^{-4}$–10^{-3} for $u_p = 0.25$–1.75 km/s. However, peak strain rates in hard phase simulations are notably larger for Hugoniostat shocks than for explicit impacts. The Hugoniostat gives a peak rate $\sim 2 \times 10^{-3}$ at $u_p = 1.5$ km/s compared to $\sim 6 \times 10^{-4}$ for the explicit impact at a similar u_p. We attribute the larger strain rate of Hugoniotstat shocks to the overdamped relaxation of the barostat employed. The lack of inertia in the barostat results in a nearly instantaneous peak strain rate that monotonically decays, while real impacts result in a pulse shape that gradually ramps up and then ramps down the strain rate. Since the Hugoniostat only displays the ramp down portion of this profile but must reach the same compression over a similar timescale, it will tend to display a higher initial strain rate.

B. Normal stress evolution

The different strain rate profiles imposed by Hugoniostat and explicit impact methods induce different paths through thermodynamic state space during loading. We measure these paths by plotting the parametric curve $\sigma_{xx}(t)$ versus $\rho_0/\rho(t)$ for material undergoing shock. For a steady shock front, the trajectory along the waveform is constrained to a path called the Rayleigh line [61]. In σ_{xx} - ρ^{-1} space, the Rayleigh lines are linear.

Figures 8(a) and 8(b) plot the shock trajectories for explicit impacts. Trajectories follow the expected linear path from the quiescent state to the Hugoniot curve indicated by a red dashed line. The symbols in Fig. 8 are spaced at regular time intervals and show that the material transits rapidly up the Rayleigh but slows its ascent as it approaches the Hugoniot. We also observe a slight deviation from linearity, with trajectories displaying a negative curvature towards their final Hugoniot states. This indicates that the materials display a time-dependent mechanical response. At early times, they have a stiffer mechanical response, following a steeper Rayleigh line, before relaxing as systems approach their Hugoniot states. The slope of the Rayleigh lines is

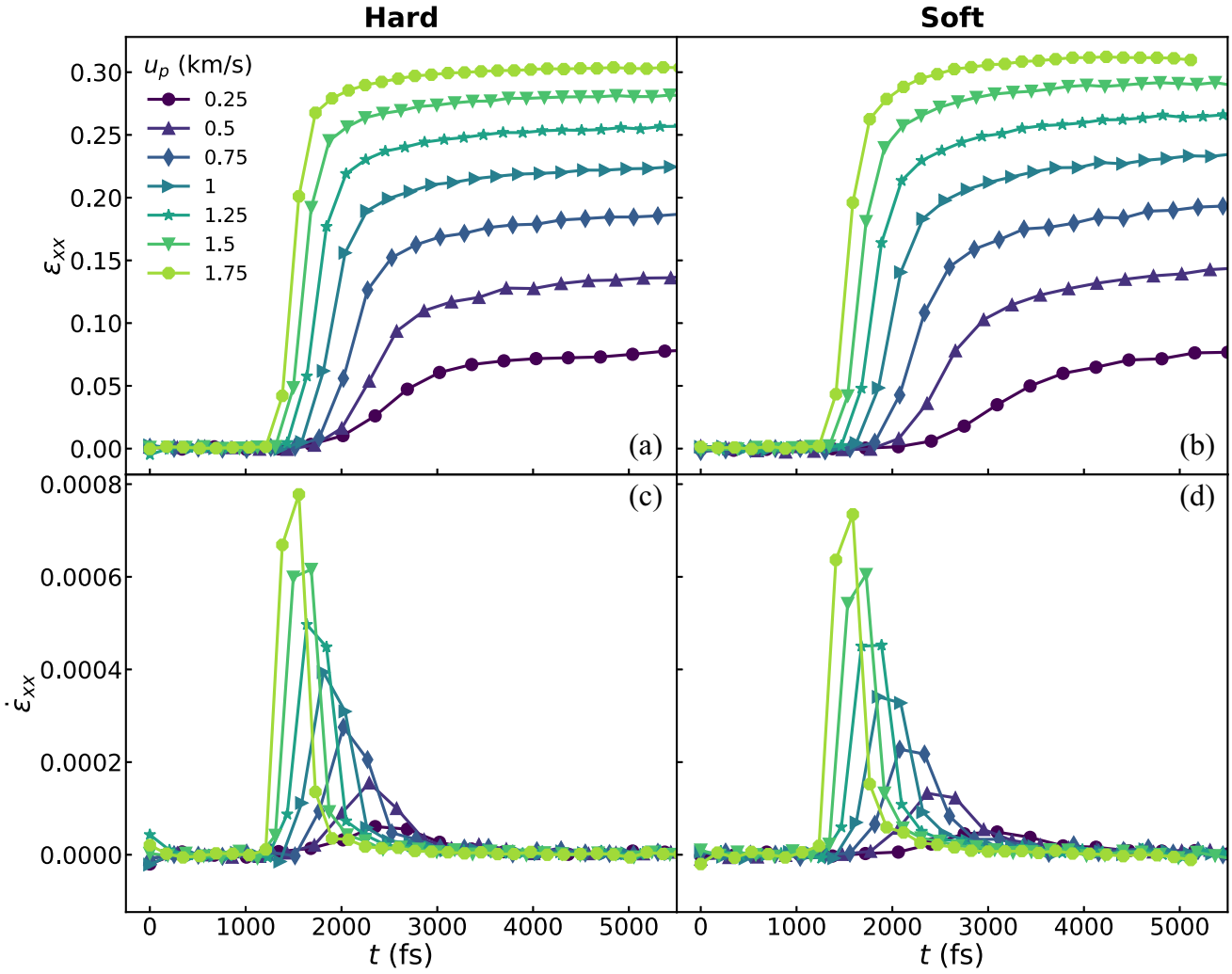

FIG. 6. [(a) and (b)] Engineering strain ϵ_{xx} and [(c) and (d)] strain rate $\dot{\epsilon}_{xx}$ vs time t for hard (left) and soft (right) phase systems imposed by shock waves during explicit impacts for varying particle velocity u_p.

proportional to the shock speed u_s, which we find increases linearly with u_p.

The thermodynamic paths produced from Hugoniostat simulations are more complex and do not follow a straight Rayleigh line. Figures 8(c) and 8(d) plot the evolution of the normal stress with respect to density for all Hugoniostat shocks, along with the developed Hugoniot curves for each system. For all shocks, we observe that the loading profiles shown in Fig. 7 result in nonlinear trajectories. This is unsurprising, as our Hugoniostat method does not subject the material to the loading profile imposed by a steady structured shock and does not need to satisfy the strict conservation relations imposed on a physically propagating shock. Although Hugoniostat shocks are not linearly constrained within phase space, the multiscale shock technique developed by Reed *et al.* [30] is an alternative equilibrium shock method that forces systems to evolve along the Rayleighu line.

C. Shock Hugoniots

To compare the shock responses for both methods, we first plot the Hugoniot temperatures T and normal stresses σ_{xx} versus u_p in Fig. 9 for both hard and soft systems. Both methods produce nearly identical thermal and normal stress responses over the full range of u_p. Soft phases show a slight enhancement of σ_{xx} and depression in T post-shock, giving a first indication that less plastic relaxation has occurred on the timescale of the explicit impact simulations than for the longer Hugoniostat simulations. Below, we verify this claim and show that it is a significant effect.

Despite predicting similar σ_{xx} and T at fixed u_p, Fig. 10(a) shows the methods give markedly different shock velocities u_s versus u_p. At all velocities, explicit impacts have u_s systematically elevated above Hugoniostat predictions. In addition, explicit impacts only resolve a linear $u_s \propto u_p$ Hugoniot relationship, whereas Hugoniostat simulations resolve lower speeds and nonlinear deviations for weak shocks. From Eq. (1), u_s depends on both the jump in normal stress and specific volume of the material. Given that we observe similar σ_{xx} for both methods in Fig. 9, the systems must be compressed to different densities. This is indeed shown in Fig. 10(b), with Hugoniostat simulations resulting in small ($\sim$5%) but significant increases in density relative to explicit impacts.

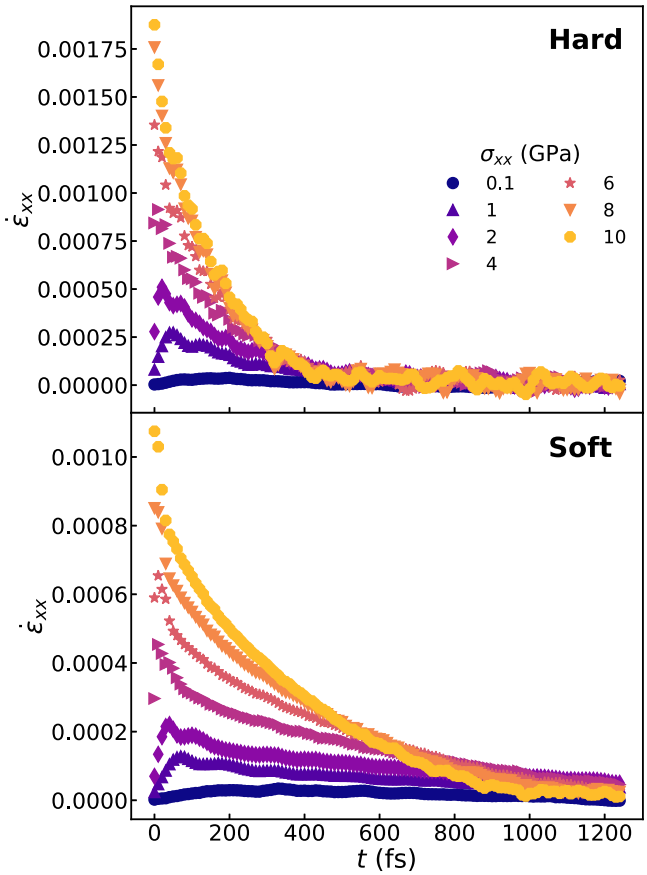

FIG. 7. Engineering strain rate $\dot{\epsilon}_{xx}$ vs time t for hard (top) and soft (bottom) phase systems from Hugoniostat simulations for varying normal stress σ_{xx}. The time axis is truncated to 1.25 ps from the total 20 ns of simulation time to highlight initial transient region.

Our results show that explicit impacts are not resolving identical post-shock states on the relatively short timescales on which they can be simulated. Further, these differences lead to large differences in the predicted shock speeds. Hugoniostat simulations resolve post-shock states for times ∼10 ns, which was found to be sufficient for the material states to converge, while impact simulations are limited by the size of the sample to times ∼10 ps. As such, material in explicit impacts likely lacks sufficient time to mechanically relax to a higher density post-shock state such that the transiting front is not fully developed.

D. Shear stress relaxation

For glassy polymers, relaxation is controlled by the cooperative plastic rearrangement of polymer backbones, which often occurs slowly through activated creep mechanisms. To quantify plastic relaxation in the post-shock state, we measure a deviatoric shear stress $\tau = \sigma_{xx} - \frac{1}{2}(\sigma_{yy} + \sigma_{zz})$ We track the time evolution $\tau(t)$ by measuring the stress at fixed distances behind the transiting front. Figure 11 plots τ versus time elapsed in the post-shock state for all explicit impact simulations. τ increases rapidly and peaks near the center of the front at $t = 0$. The peak value of τ increases with increasing normal load σ_{xx}, exceeding the yield stress of the quiescent materials. This is a manifestation of the enhanced yield strength of glassy polymers under pressure and at high rates [62]. Behind the front, the shear stress rapidly decreases, but the rate of decay slows continually, displaying a logarithmic decay. Figure 12 plots $\tau(t)$ for all Hugoniostat shocks. The shear stresses peak at higher values than for explicit impacts, consistent with the higher strain rates measured in Fig. 7. Despite this, $\tau(t)$ shows the same form of logarithmic decay as observed in explicit impacts, indicating that both simulation protocols are resolving qualitatively similar plastic relaxation processes.

To model and compare stress relaxation across systems and conditions, we fit $\tau(t)$ to a stress-activated Eyring model. The relevant expression derived by Guiu and Pratt is [63]

$$\tau(t) = \tau_0 - \tau_V \ln\left(1 + \frac{\dot{\tau}_0}{\tau_V} t\right), \tag{4}$$

which predicts a logarithmic decay of the initial stress τ_0 with a characteristic Eyring stress scale:

$$\tau_V = \frac{k_B T}{V_*}, \tag{5}$$

The activation volume V_* describes the susceptibility of the relaxation mechanism to the shear stress τ. For fitting, we fixed $\tau_0 = \tau(t = 0)$, while τ_V and $\dot{\tau}_0$ are optimized using the Levenberg-Marquardt algorithm [64]. Results from both Hugoniostat and impact simulations can be modeled by fits to Eq. (4) and are plotted as dashed curves in Figs. 11 and 12. This indicates that the plastic relaxation of both phases during shock can be understood as a single stress-biased thermally activated process.

The fit values for τ_V and $\dot{\tau}_0$ are plotted versus σ_{xx} in Fig. 13 for all systems. Both parameters increase with σ_{xx}, and we obtain roughly similar values for the hard and soft phases. Both hard and soft systems show Eyring stresses $\tau_V \sim 50$–150 MPa. These are close to typical yield stresses for glassy polymers, suggesting that the stress relaxation in both shock-compressed phases is mediated by the same local plastic rearrangements that mediate yield in glassy polymers. Thus despite the hard and soft phases displaying glassy and rubbery properties in equilibrium, respectively, both exhibit similar glassy mechanics when immobilized under high pressures.

The localized scale of the plastic relaxation process is supported by plotting the activation volume $V_* = \tau_V / k_B T$ in Fig. 14. Our data suggest that soft systems might display smaller V_* than hard systems, which would make sense given the greater flexibility of the soft-domain molecules, but these differences are subtle and too noisy for us to report with confidence. What is clear is that both domains rapidly converge to a small $V_* \sim 0.1$ nm^3 or less above $\sigma_{xx} \sim 2$ GPa. This corresponds to a length scale ∼0.46 nm, which is of the size of 1-2 monomers of the chain backbone.

Our analysis shows that both simulation methods produce the same thermomechanical response and stress relaxation in both polymer phases. To directly visualize this, we compare relaxation curves from both methods for shocks of similar normal load σ_{xx} in Fig. 15. The explicit impact data are horizontally shifted in time so that their initial τ_0 coincides with the same stress value on the corresponding curve from

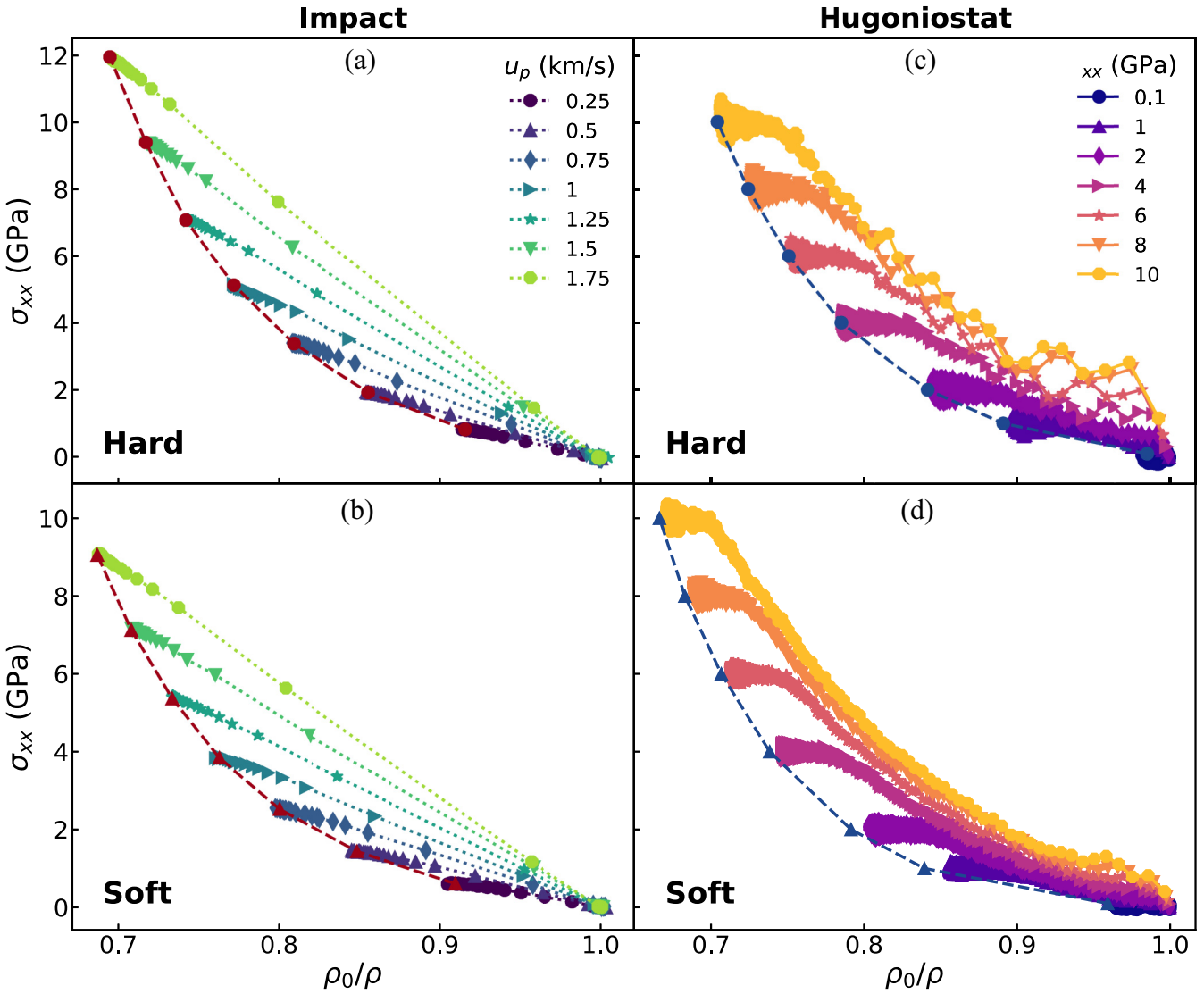

FIG. 8. Evolution of normal stress σ_{xx} vs relative density ρ_0/ρ for hard and soft phases at varying particle velocity u_p during [(a) and (b)] explicit impact shock simulations and varying normal stress σ_{xx} for [(c) and (d)] Hugoniostat shock simulations. Red and blue curves represent the shock Hugoniots from explicit impact and Hugoniostat simulations, respectively. Dotted lines on the left panels represent the Rayleigh lines connecting the quiescent and shock Hugoniot states.

Hugoniostat simulations. We find that the relaxation curves show overlapping stress relaxation when different methods share the same σ_{xx}, T, and τ states.

For any practical atomic simulation, the Hugoniostat Hugoniot states in Figs. 9 and 10 represent much more relaxed systems compared to those of explicit impacts due to an underlying difference in the simulation timescales. Instead, they indicate the influence of the residual shear stress on the apparent shock response of these polymers. τ decays logarithmically and as a result converges much slower behind the front compared to the hydrostatic pressure or temperature. This residual τ prevents the material from compacting to a higher density.

This characteristic shear stress relaxation exhibited by our models has also been observed in several other MD shock simulations of glassy polymers [22,49]. However, it is unclear whether this Eyring-like stress relaxation is unique to high-rate shock impacts or simply representative of conventional glassy creep at elevated pressures and temperatures. To investigate this, we also perform similar measurements of the shear stress at thermodynamic states comparable to shocks when subjected to quasistatic loading. It is not possible for quasistatic loading to exactly reproduce the states along the shock Hugoniot. Therefore we simulate systems at shear stresses and temperatures similar to those of the shocked states in Fig. 15 for $u_p = 1.5$ km/s. We take our cubic models at their equilibrium densities under ambient conditions and perform a uniaxial strain compression at a true strain rate of 10^{-6} fs^{-1} until the shear stress reaches a value of 0.8/1.1 GPa for the hard/soft phase. Afterwards, the temperature is raised to 526 and 517 K for the hard and soft phases, respectively. This produces quasistatic states with T and τ comparable to those generated ∼1 ps behind the shock front. These results are plotted as squares in Fig. 15, and show a comparably slow

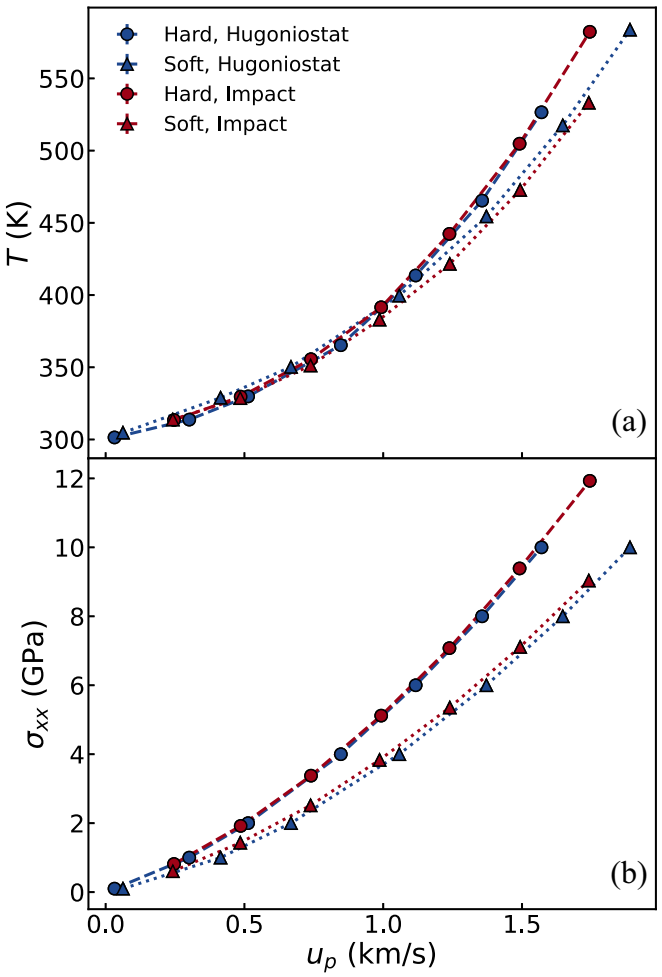

FIG. 9. (a) Temperature T and (b) normal stress σ_{xx} vs particle velocity u_p for the hard and soft phases from Hugoniostat (blue) and explicit impact (red) shock simulations.

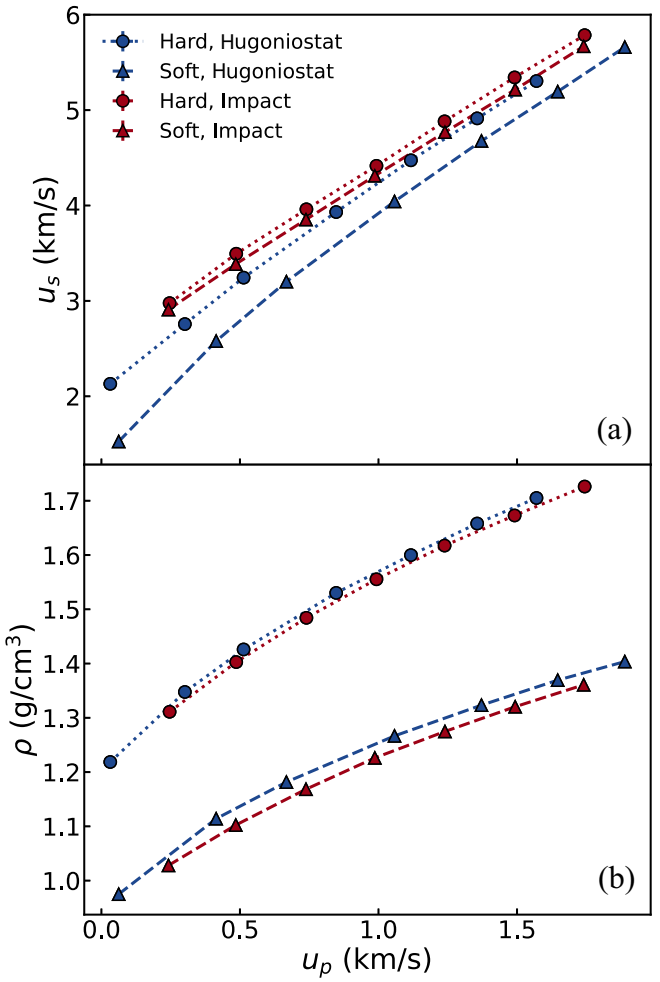

FIG. 10. (a) Shock velocity u_s and (b) density ρ vs particle velocity u_p for the hard and soft phases from Hugoniostat and explicit impact simulations.

stress relaxation. Fitting the stress to Eq. (5) results in volumes of $V_* = 0.07/0.10$ nm^3 for the hard/soft phase, which is comparable to a few monomers' volume. This suggests that the same local monomeric rearrangements mediate the terminal stress relaxation of these highly pressurized glassy polymers when subjected to either quasistatic or high-rate shock loading.

E. Molecular plasticity

The localized scale of plasticity inferred by the Eyring model is directly corroborated by measurements of atomic rearrangements on the molecular scale. To quantify local irreversible shear transformations during deformation, we use the method formulated by Falk and Langer [65] to compute the nonaffine squared displacement D^2_{min}, a metric that represents local atomic deviations from affine deformation. A cutoff radius of 1 nm is used to compute the atomic deformation gradient tensor for each atom. Figure 16 plots the nonaffine squared displacements D^2_{min} versus the distance behind the shock front for all explicit impact shocks. In the quiescent material at $x_{BF} < 0$, there is a nonzero baseline value of D^2_{min} in each phase that corresponds to the equilibrium aging of the glass. At the front, the plasticity rapidly peaks as the material is deformed above its yield strength by the shock. Beyond this point, D^2_{min} subsequently decays with increasing distance behind the front and appears to eventually reach a steady state associated with the aging of the glass at elevated pressures and temperatures post-shock.

To illustrate the correspondence between the shear stress relaxation and local atomic nonaffine squared displacements behind the front, we simultaneously overlay shear stress relaxation curves $\tau(x_{BF})$ for $u_p = 1.75$ km/s in Fig. 16. The initial sharp decline in τ coincides closely with the decrease in D^2_{min} behind the front. As the stress relaxation transitions towards its terminal logarithmic rate, we observe a corresponding stabilization in the rate of plastic rearrangements. While not explicitly shown, we have found that these trends persist across all u_p for both phases. These similarities in the characteristic time and length scales of these curves further highlight the role of local molecular rearrangements in the plastic relaxation of these glassy polymers.

Several previous studies have suggested that the shock-induced disruption of directional bonds in the hard phase may

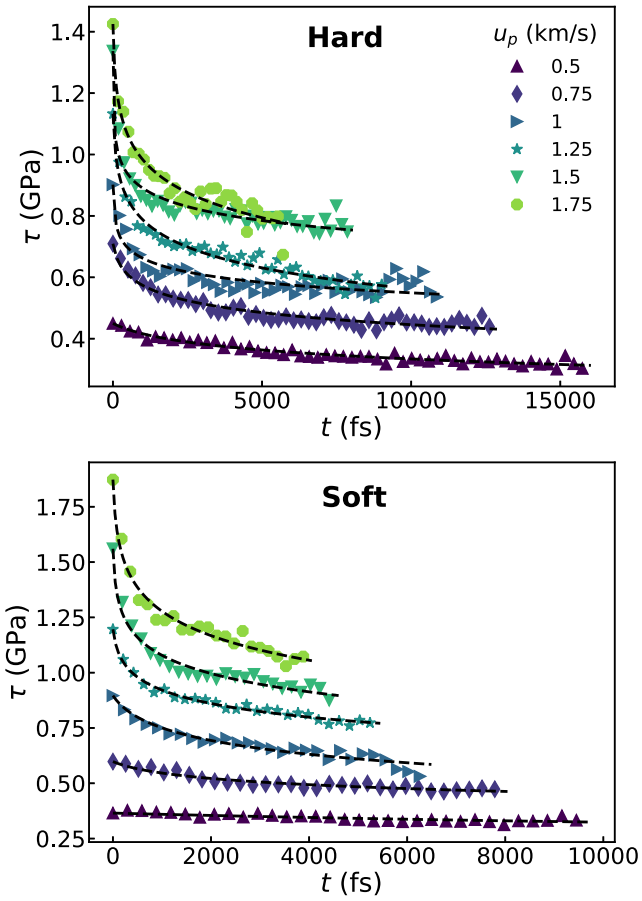

FIG. 11. Shear stress τ vs time t elapsed since shock for all explicit impact shocks. Dashed black lines illustrate fits of data to Eq. (4).

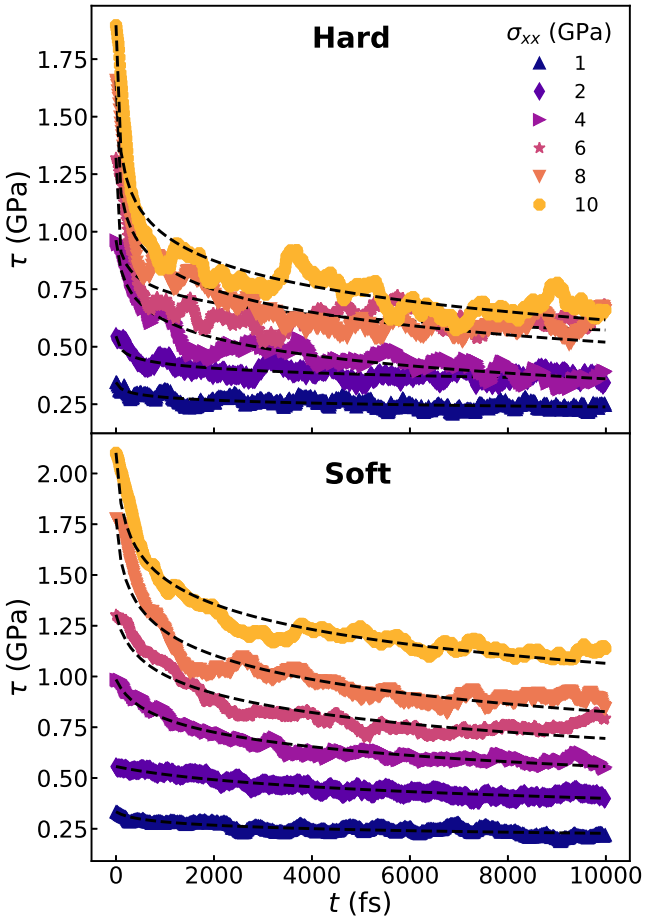

FIG. 12. Shear stress τ vs time t elapsed since shock for all Hugoniostat shocks. The original data are smoothed by applying a Savitsky-Golay filter to yield the plotted curves. The time axis is truncated to 5 ps from the total 20 ns of simulation time to highlight the initial transient region. Dashed black lines illustrate fits of data to Eq. (4).

be related to energy dissipation in polyurea [9,10,15]. Using a pure hard phase constituent model, Manav *et al.* [15] found that increasing shock pressure resulted in increased hydrogen bond dissociation and the distortion of phenyl rings participating in π–π stacking. However, it is unclear whether these processes are dynamic and/or coupled to the transient plasticity observed in our models. To investigate the time-dependent nature of these directional bonds, we probe for changes in the coordination of hydrogen bonds across timescales using both Hugoniostat and explicit impact simulations. To quantify changes in structure, we compute the radial distribution function of oxygen and hydrogen atoms $g(r)_{\text{O-H}}$ that form hydrogen bonds within the hard phase, whilst the coordination of intramolecular species is omitted from the calculation. Figure 17 compares the $g(r)_{\text{O-H}}$ curves from Hugoniostat and impact shocks with similar impact strength $u_p \approx 1.5$ km/s. The equilibrium structure is also characterized and plotted for reference with shocked states. The leftmost peak, at $r \approx 1.9$ Å, represents the coordination of oxygen and hydrogen atoms that form hydrogen bonds between intermolecular urea groups. For strong shocks with both methods, we observe both a decrease in the peak height and position relative to the equilibrium structure. This indicates the breaking of these directional bonds as the hard phase is compacted during loading. We find that this occurs very rapidly over a subpicosecond timescale, with $g(r)_{\text{O-H}}$ curves remaining relatively unchanged when sampled across longer time intervals. This shows that hydrogen bond rearrangement is rapid and only active during the initial compression imposed by the shock and does not contribute to long-term stress relaxation.

F. Short timescale thermodynamics

While the Hugoniostat can more efficiently resolve long-time relaxation behavior, it is unlikely that these relaxed states are actually realized in real nanostructured materials during shock impact. Scattering experiments indicate that typical interdomain spacings within a typical polyurea microstructure are of the order 5–10 nm [3]. This is comparable to the shock width, and for $u_s \sim 1$ km/s, a front would transit such a domain in ∼10 ps. At longer timescales, interactions between the shock and interface boundaries will produce additional reflected shocks that can further disrupt the local material thermodynamic state. Thus, the transient states resolved by explicit impact simulations on the picosecond timescale are more representative of the material response on the nanoscale than the steady-state response of the Hugoniostat.

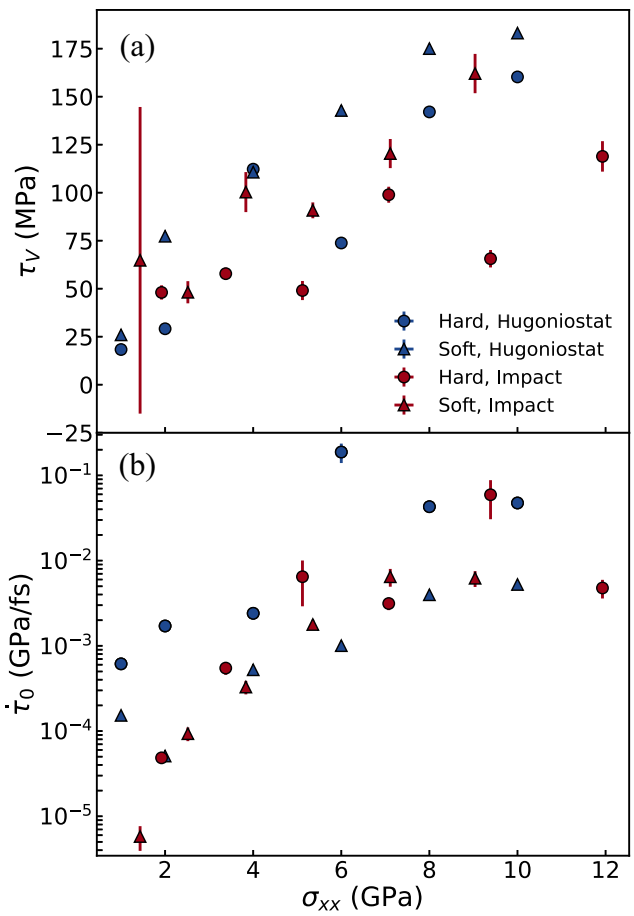

FIG. 13. (a) Activation stress τ_V and (b) initial shear stress relaxation rate $\dot{\tau}_0$ fit parameters for Eq. (4) plotted vs normal stress σ_{xx} for all shocks.

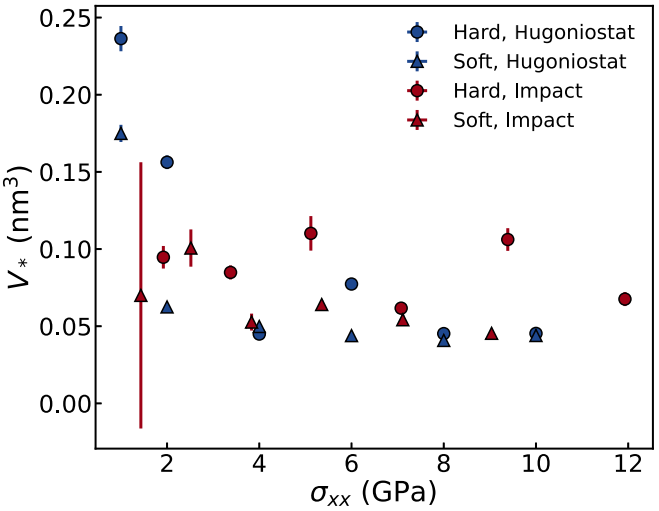

FIG. 14. Activation volume V_* vs normal stress σ_{xx} for all shocks. Both hard and soft domains show similar V_* at elevated pressure, indicating similar local relaxation under large compaction.

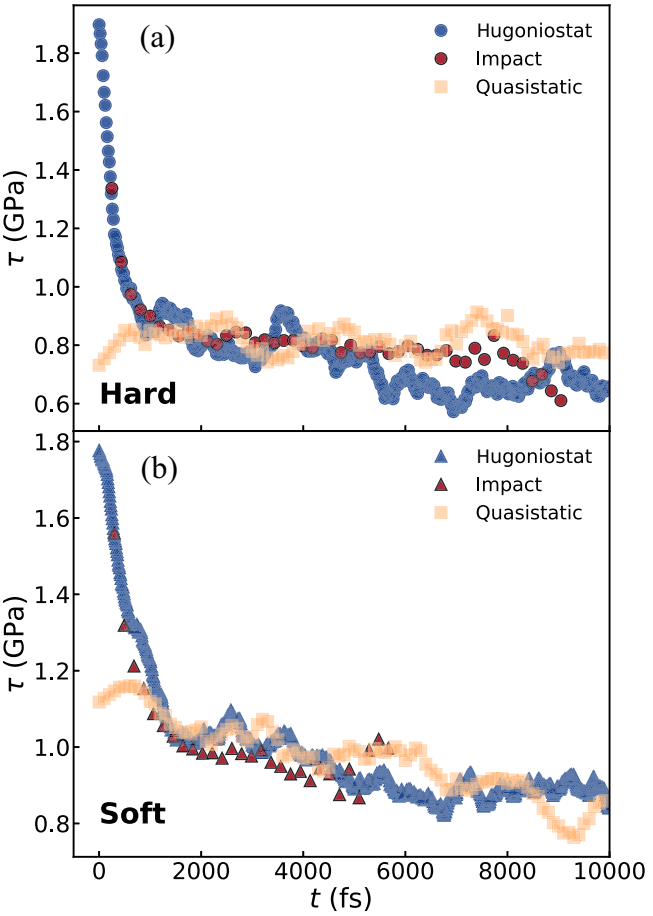

FIG. 15. Shear stress τ vs time t of shocked (a) hard and (b) soft phase material from Hugoniostat and explicit impact shocks. Systems are chosen for comparison between methods based upon similar shock intensity. For the hard phase, we pick a Hugoniostat simulation with $\sigma_{xx} = 10$ GPa and explicit impact shock with $u_p = 1.5$ km/s. For the soft phase, we pick a Hugoniostat simulation with $\sigma_{xx} = 8$ GPa and explicit impact shock with $u_p = 1.5$ km/s. Explicit impact data are horizontally shifted to overlap the peak shear stress along the Hugoniostat curve. Yellow data represent $\tau(t)$ from quasistatic uniaxial compression simulations at comparable shear stresses to shocks.

Given our understanding that both methods induce a similar time-dependent plasticity, we predict that selective averaging of transient Hugoniostat data on a shorter timescale will also lead to a better convergence of other thermodynamic and hydrodynamic variables with explicit impacts. To test this, we average ρ and u_s from Hugoniostat simulations over $t \in [10, 20]$ ps and $t \in [5, 15]$ ps for the hard and soft phases, respectively. Figure 18 compares these data across all shocks with those of our explicit impacts. In panel (b), we now observe near perfect agreement between the $\rho(u_p)$ curves for both methods. This supports our claim that the discrepancies in post-shock densities in Fig. 10(b) were due to the increased plasticity resolved in our longer Hugoniostat simulations. Despite a better agreement in ρ, Fig. 18(a) still shows that explicit impacts predict a systematically higher u_s and stiffer response. This is notable since the jump conditions in Eqs. (1) and (2) relate u_s and u_p to σ_{xx}, P_0, v,

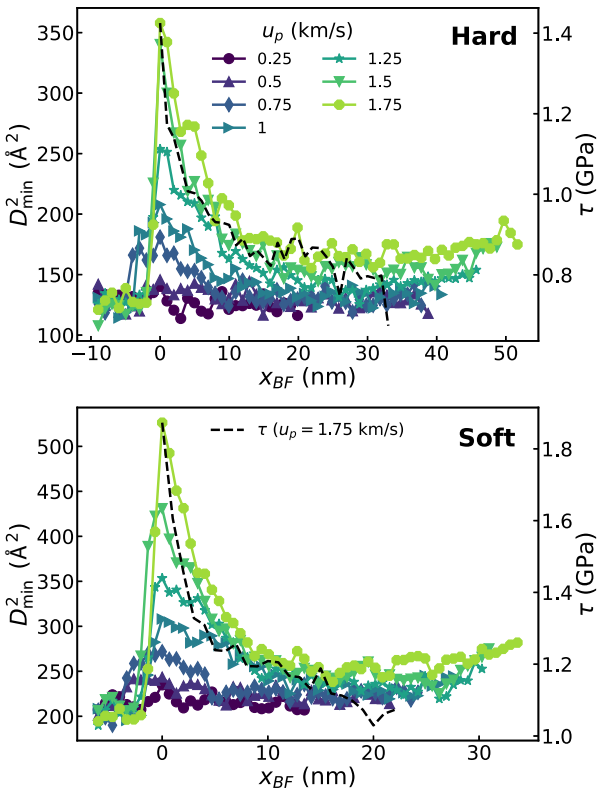

FIG. 16. Nonaffine squared displacement $D^2_{\min}$ profiles of hard and soft phase material during explicit impact shocks for all u_p. Hard and soft profiles shown are at 13 and $t = 9$ ps after impact, respectively, and are plotted as a function of the distance behind the shock front x_{BF}. Black dashed lines indicate the shear stress τ as a function of x_{BF} for $u_p = 1.75$ km/s.

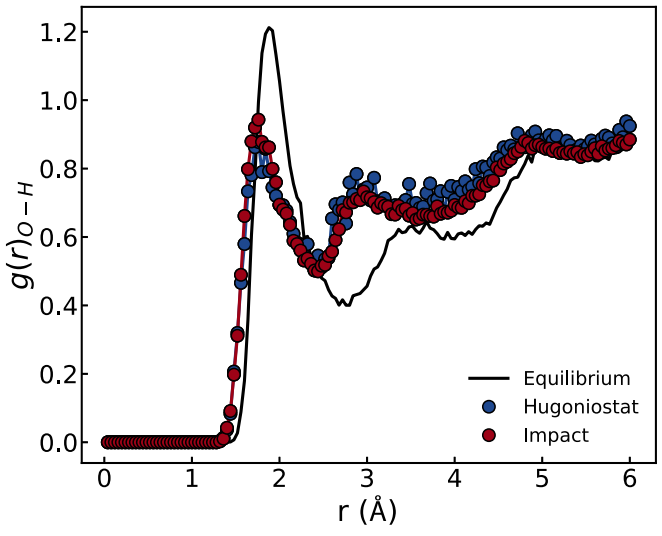

FIG. 17. Radial distribution function $g(r)_{\text{O-H}}$ of oxygen and hydrogen atoms in the hard phase for equilibrium and post-shock Hugoniostat and explicit impact shock configurations. Curves for shock simulations are averaged over a post-shock time interval of $t \in [1, 5]$. A Hugoniostat shock of $\sigma_{xx} = 10$ GPa and impact shock of $u_p = 1.5$ km/s were chosen for similar shock intensities. Intramolecular contributions to the RDF are omitted to isolate intermolecular contributions from hydrogen bonds.

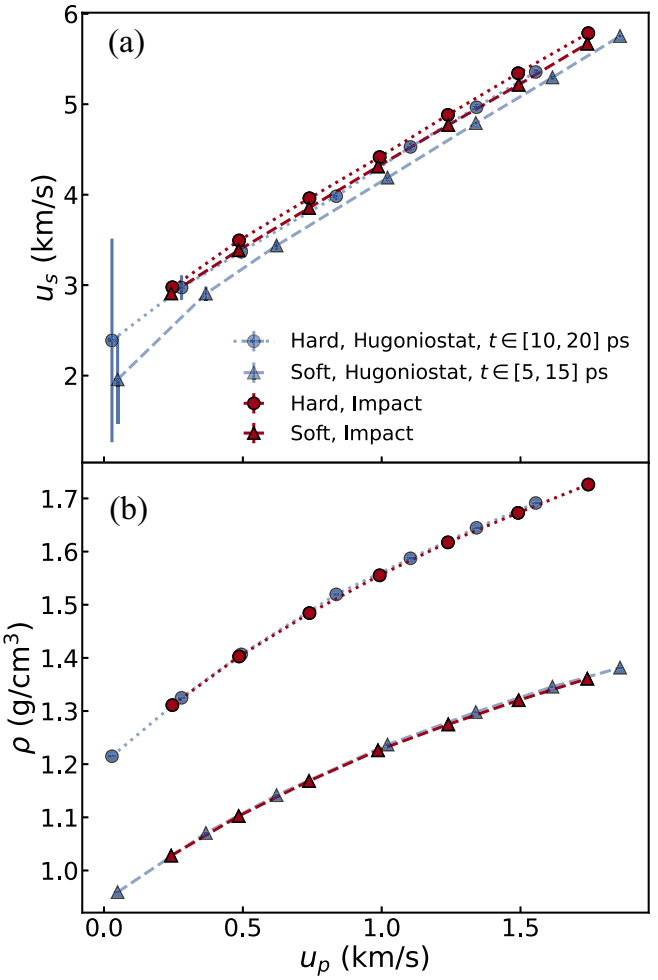

FIG. 18. (a) Shock velocity u_s and (b) density ρ vs particle velocity u_p for the hard and soft phases from Hugoniostat and explicit impact simulations. Hugoniostat data are time averaged across $t \in [10, 20]$ ps and $t \in [5, 15]$ ps for the hard and soft phases, respectively.

and v_0, all of which are now identical between both methods. However, these equations are only valid for a stationary front in a steady state. As a result, the curves in Fig. 18(a), computed from a transient state, do not predict the transient shock speeds of developing fronts in explicit impact simulations.

IV. CONCLUSION

We applied molecular dynamics simulations to study the shock response of representative volume elements of hard and soft molecular phases within nanostructured polyurea using both Hugoniostat and explicit impact simulation methods. Hugoniostat simulations resolve post-shock states over durations of many nanoseconds, but explicitly impacts are limited by system size to tens of picoseconds. Despite these differences, we find good agreement between the temperature and the normal stress σ_{xx} for both methods, suggesting that these quantities rapidly equilibrate behind the shock front. In contrast, the deviatoric stress τ exhibits an Eyring-like shear stress relaxation associated with a logarithmically decaying

rate of stress-activated plastic deformation. The slow relaxation of τ coincides with a slow compaction of the post-shock density. Hugoniostat shocks can be simulated for sufficiently long times to relax the shear stress τ to a steady-state value. However, explicit impact simulations are constrained to significantly shorter timescales, leading to the measurement of transient shocked states with significantly higher residual shear stress.

Despite the stark differences in the chemistry and mechanical properties under ambient conditions between the hard and soft phases, both systems displayed similar glassy plasticity under strong shocks. The measured Eyring stresses were on the order of the typical yield stress of glassy polymers ∼100 MPa, indicating that local plastic rearrangements control the stress relaxation of both phases similar to the yielding of glasses. This is further supported by the comparable activation volumes of the hard and soft domains. The length scales of plastic events are confined to regions that are no larger than a few atoms in size. Despite the increased cohesion due to hydrogen bonding and aromatic moieties in the hard phase, the influence of these groups becomes suppressed at the high densities imposed by shocks.

Steady shock speeds predicted by the Hugoniostat are noticeably slower than those of propagating shocks measured in explicit impacts, even when compared on comparable timescales such that the post-shock values of T, σ_{xx}, τ, and ρ are matched. We attribute this disagreement to the fact that the Hugoniostat methodology uses the steady-state Hugoniot relationships to compute u_s from the instantaneous post-shock state. This relationship cannot be assumed to hold during the transient development of a front, which our results show is a slow process in these glassy systems.

For a properly parameterized Hugoniostat simulation, we find that shocks faithfully reproduce the thermomechanics of plastic deformation and stress relaxation behind the shock front. Thus the Hugoniostat is an effective tool for predicting the long-time damage accumulation in a PU material after shock. However, the shock speed u_s predicted by the Hugoniostat is only accurate in the long-time limit, and this steady-state is almost certainly never achieved in a real PU microstructure. Indeed, shocks of this magnitude will transit the hard/soft domains on timescales ∼10–100 ps, but shear stresses relax over nanoseconds. Thus, we would expect shocks in PU to be propagated by unsteady waves that frequently reflect and transmit at domain interfaces. Thus, if practical shock impedances $Z = \rho u_s$ are needed to predict shock scattering off heterogeneous microstructures [61,66], the Hugoniostat is unlikely to provide an accurate value. From just our Hugoniostat measurements, one would predict a much larger impedance mismatch than that actually experienced by the shock given our data. This underscores the continued need for explicit impact simulations to characterize the empirical shock response of glassy polymer systems.

ACKNOWLEDGMENTS

The authors would like to thank Christine C. Roberts, Brad H. Jones, and Joel T. Clemmer for valuable discussions and advice during the course of this project. This research was supported by Sandia National Laboratories Lab-Directed Research and Development through Contract No. 2564938.

DATA AVAILABILITY

The data that support the findings of this article are openly available [67], embargo periods may apply.

[1] N. Iqbal, M. Tripathi, S. Parthasarathy, D. Kumar, and P. K. Roy, Polyurea coatings for enhanced blast-mitigation: A review, RSC Adv. **6**, 109706 (2016).

[2] N. Iqbal, P. Sharma, D. Kumar, and P. Roy, Protective polyurea coatings for enhanced blast survivability of concrete, Constr. Build. Mater. **175**, 682 (2018).

[3] V. Agrawal, K. Holzworth, W. Nantasetphong, A. V. Amirkhizi, J. Oswald, and S. Nemat-Nasser, Prediction of viscoelastic properties with coarse-grained molecular dynamics and experimental validation for a benchmark polyurea system, J. Polym. Sci. Part B: Polym. Phys. **54**, 797 (2016).

[4] M. Grujicic, B. P. d'Entremont, B. Pandurangan, J. Runt, J. Tarter, and G. Dillon, Concept-level analysis and design of polyurea for enhanced blast-mitigation performance, J. Mater. Eng. Perform. **21**, 2024 (2012).

[5] C. E. Carraher, *Seymour/Carraher's Polymer Chemistry* (CRC Press, Boca Ranton, 2003).

[6] W. Mock, S. Bartyczak, G. Lee, J. Fedderly, and K. Jordan, in *Proceedings of the American Physical Society Topical Group on Shock Compression of Condensed Matter*, edited by M. L. Elert, W. T. Buttler, M. D. Furnish, W. W. Anderson, and W. G. Proud (AIP Publishing, Melville, 2009), pp. 1241–1244.

[7] A. H. Pacheco, R. L. Gustavsen, T. D. Aslam, and B. D. Bartram, in *Proceedings of the Conference of the American Physical Society Topical Group on Shock Compression of Condensed Matter*, edited by R. Ravelo, T. Sewell, R. Chau, T. Germann, I. I. Oleynik, and S. Peiris (AIP Publishing, Melville, 2015) p. 120029.

[8] A. Haris, H. P. Lee, and V. B. C. Tan, An experimental study on shock wave mitigation capability of polyurea and shear thickening fluid based suspension pads, Def. Technol. **14**, 12 (2018).

[9] M. Grujicic, B. Pandurangan, W. Bell, B. Cheeseman, C.-F. Yen, and C. Randow, Molecular-level simulations of shock generation and propagation in polyurea, Mater. Sci. Eng. A **528**, 3799 (2011).

[10] M. Grujicic, R. Yavari, J. S. Snipes, S. Ramaswami, J. Runt, J. Tarter, and G. Dillon, Molecular-level computational investigation of shock-wave mitigation capability of polyurea, J. Mater. Sci. **47**, 8197 (2012).

[11] B. Arman, A. S. Reddy, and G. Arya, Viscoelastic properties and shock response of coarse-grained models of multiblock versus diblock copolymers: insights into dissipative properties of polyurea, Macromolecules **45**, 3247 (2012).

[12] S. Heyden, M. Ortiz, and A. Fortunelli, All-atom molecular dynamics simulations of multiphase segregated polyurea under quasistatic, adiabatic, uniaxial compression, Polymer **106**, 100 (2016).
[13] M. Liu and J. Oswald, Coarse–grained molecular modeling of the microphase structure of polyurea elastomer, Polymer **176**, 1 (2019).
[14] K. Yao, Z. Liu, T. Li, B. Guo, and Z. Zhuang, Mesoscale structure-based investigation of polyurea dynamic modulus and shock-wave dissipation, Polymer **202**, 122741 (2020).
[15] M. Manav and M. Ortiz, Molecular dynamics study of the shock response of polyurea, Polymer **212**, 123109 (2021).
[16] K. Yao, D. Chu, T. Li, Z. Liu, B.-H. Guo, J. Xu, and Z. Zhuang, Atomic-scale simulation of Hugoniot relations and energy dissipation of polyurea under high-speed shock, Eng. Comput. **38**, 1209 (2021).
[17] M. A. N. Dewapriya and R. E. Miller, Molecular dynamics simulations of shock propagation and spallation in amorphous polymers, J. Appl. Mech. **88**, 101005 (2021).
[18] M. Dewapriya and R. Miller, Quantum and classical molecular dynamics simulations of shocked polyurea and polyurethane, Comput. Mater. Sci. **203**, 111166 (2022).
[19] T. R. Mattsson, J. M. D. Lane, K. R. Cochrane, M. P. Desjarlais, A. P. Thompson, F. Pierce, and G. S. Grest, First-principles and classical molecular dynamics simulation of shocked polymers, Phys. Rev. B **81**, 054103 (2010).
[20] L. He, T. D. Sewell, and D. L. Thompson, Molecular dynamics simulations of shock waves in *cis* -1,4-polybutadiene melts, J. Appl. Phys. **114**, 163517 (2013).
[21] R. M. Elder, T. C. O'Connor, T. L. Chantawansri, Y. R. Sliozberg, T. W. Sirk, I.-C. Yeh, M. O. Robbins, and J. W. Andzelm, Shock-wave propagation and reflection in semicrystalline polyethylene: A molecular-level investigation, Phys. Rev. Mater. **1**, 043606 (2017).
[22] T. C. O'Connor, R. M. Elder, Y. R. Sliozberg, T. W. Sirk, J. W. Andzelm, and M. O. Robbins, Molecular origins of anisotropic shock propagation in crystalline and amorphous polyethylene, Phys. Rev. Mater. **2**, 035601 (2018).
[23] L. Liao, X. Wang, and C. Huang, Molecular insights into shock responses of amorphous polyethylene, Modell. Simul. Mater. Sci. Eng. **29**, 015008 (2021).
[24] C. A. Lemarchand, Molecular dynamics simulations of several linear homopolymers: Assessment and comparison of shock properties, Polymer **290**, 126524 (2024).
[25] B. L. Holian, W. G. Hoover, B. Moran, and G. K. Straub, Shock-wave structure via nonequilibrium molecular dynamics and Navier-Stokes continuum mechanics, Phys. Rev. A **22**, 2798 (1980).
[26] V. V. Zhakhovskii, K. Nishihara, and S. I. Anisimov, Shock wave structure in dense gases, J. Exp. Theor. Phys. Lett. **66**, 99 (1997).
[27] B. L. Holian and P. S. Lomdahl, Plasticity induced by shock waves in nonequilibrium molecular-dynamics simulations, Science **280**, 2085 (1998).
[28] A. V. Bolesta, L. Zheng, D. L. Thompson, and T. D. Sewell, Molecular dynamics simulations of shock waves using the absorbing boundary condition: A case study of methane, Phys. Rev. B **76**, 224108 (2007).
[29] V. V. Zhakhovsky, M. M. Budzevich, N. A. Inogamov, I. I. Oleynik, and C. T. White, Two-zone elastic-plastic single shock waves in solids, Phys. Rev. Lett. **107**, 135502 (2011).
[30] E. J. Reed, L. E. Fried, and J. D. Joannopoulos, A method for tractable dynamical studies of single and double shock compression, Phys. Rev. Lett. **90**, 235503 (2003).
[31] J.-B. Maillet, M. Mareschal, L. Soulard, R. Ravelo, P. S. Lomdahl, T. C. Germann, and B. L. Holian, Uniaxial Hugoniostat: A method for atomistic simulations of shocked materials, Phys. Rev. E **63**, 016121 (2000).
[32] R. Ravelo, B. Holian, T. Germann, and P. Lomdahl, Constant-stress Hugoniostat method for following the dynamical evolution of shocked matter, Phys. Rev. B **70**, 014103 (2004).
[33] M. Grujicic and B. Pandurangan, Mesoscale analysis of segmental dynamics in microphase-segregated polyurea, J. Mater. Sci. **47**, 3876 (2012).
[34] M. Grujicic, J. S. Snipes, S. Ramaswami, R. Yavari, and M. K. Ramasubramanian, Meso-scale computational investigation of shock-wave attenuation by trailing release wave in different grades of polyurea, J. Mater. Eng. Perform. **23**, 49 (2014).
[35] V. Agrawal, G. Arya, and J. Oswald, Simultaneous iterative Boltzmann inversion for coarse-graining of polyurea, Macromolecules **47**, 3378 (2014).
[36] D. J. Pastine, P, v, T equation of state for polyethylene, J. Chem. Phys. **49**, 3012 (1968).
[37] F. Tsou and P. C. Chou, Analytical study of Hugoniot in unidirectional fiber reinforced composites, J. Compos. Mater. **3**, 500 (1969).
[38] R. Mcqueen, S. Marsh, J. Taylor, J. Fritz, and W. Carter, The equation of state of solids from shock wave studies, *High-Velocity Impact Phenomena* (Academic Press, Cambridge, MA, 1970), pp. 293–417.
[39] G. E. Duvall and S. Taylor, JR., Shock parameters in a two component mixture, J. Compos. Mater. **5**, 130 (1971).
[40] D. Munson and K. Schuler, Steady wave analysis of wave propagation in laminates and mechanical mixtures, J. Compos. Mater. **5**, 286 (1971).
[41] L. Barker, A model for stress wave propagation in composite materials, J. Compos. Mater. **5**, 140 (1971).
[42] M. Baer and J. Nunziato, A two-phase mixture theory for the deflagration-to-detonation transition (ddt) in reactive granular materials, Int. J. Multiphase Flow **12**, 861 (1986).
[43] P. Embid and M. Baer, Mathematical analysis of a two-phase continuum mixture theory, Continuum Mech. Thermodyn. **4**, 279 (1992).
[44] A. K. Kapila, R. Menikoff, J. B. Bdzil, S. F. Son, and D. S. Stewart, Two-phase modeling of deflagration-to-detonation transition in granular materials: Reduced equations, Phys. Fluids **13**, 3002 (2001).
[45] J. L. Jordan and M. R. Baer, Mixture model for determination of shock equation of state, J. Appl. Phys. **111**, 083516 (2012).
[46] G. Young, X. Liu, C. Leng, and H. Huang, Average models for calculating the shock equation of state of alloy and mixture, Jpn. J. Appl. Phys. **58**, 066004 (2019).
[47] W. Voigt, Ueber die Beziehung zwischen den beiden Elasticitätsconstanten isotroper Körper, Ann. Phys. (NY) **274**, 573 (1889).
[48] M. Tripathi, S. Parthasarathy, D. Kumar, P. Chandel, P. Sharma, and P. K. Roy, Strain rate sensitivity of polyurea coatings: Viscous and elastic contributions, Polym. Test. **86**, 106488 (2020).

[49] G. Lecoutre, C. A. Lemarchand, L. Soulard, and N. Pineau, Hugoniostat and direct shock simulations in cis-1, 4-polybutadiene melts, Macromol. Theory Simul. **30**, 2000068 (2021).

[50] P. Wen, G. Tao, D. E. Spearot, and S. R. Phillpot, Molecular dynamics simulation of the shock response of materials: A tutorial, J. Appl. Phys. **131**, 051101 (2022).

[51] W. L. Jorgensen and J. Tirado-Rives, The OPLS [optimized potentials for liquid simulations] potential functions for proteins, energy minimizations for crystals of cyclic peptides and crambin, J. Am. Chem. Soc. **110**, 1657 (1988).

[52] W. J. Carter and S. P. Marsh, Hugoniot equation of state of polymers, Technical Report LA–13006-MS; ON: DE95016708 Los Alamos National Lab, USA, 1995.

[53] R. W. Hockney and J. W. Eastwood, *Computer Simulation Using Particles* (CRC Press, Boca Ranton, 2021).

[54] W. L. Jorgensen and J. Tirado-Rives, Potential energy functions for atomic-level simulations of water and organic and biomolecular systems, Proc. Natl. Acad. Sci. USA **102**, 6665 (2005).

[55] L. S. Dodda, J. Z. Vilseck, J. Tirado-Rives, and W. L. Jorgensen, 1.14*CM1A-LBCC: Localized bond-charge corrected CM1A charges for condensed-phase simulations, J. Phys. Chem. B **121**, 3864 (2017).

[56] L. S. Dodda, I. Cabeza de Vaca, J. Tirado-Rives, and W. L. Jorgensen, LigParGen web server: An automatic OPLS-AA parameter generator for organic ligands, Nucl. Acids Res. **45**, W331 (2017).

[57] See Supplemental Material at http://link.aps.org/supplemental/10.1103/p577-s387 for OPLS parameterization and Hugoniostat damping parameters.

[58] S. Plimpton, Fast parallel algorithms for short-range molecular dynamics, J. Comput. Phys. **117**, 1 (1995).

[59] A. M. Castagna, A. Pangon, T. Choi, G. P. Dillon, and J. Runt, The role of soft segment molecular weight on microphase separation and dynamics of bulk polymerized polyureas, Macromolecules **45**, 8438 (2012).

[60] D. E. Grady, Structured shock waves and the fourth-power law, J. Appl. Phys. **107**, 013506 (2010).

[61] L. Davison, *Fundamentals of Shock Wave Propagation in Solids* (Springer, Berlin, Heidelberg, 2008).

[62] J. Rottler and M. O. Robbins, Yield conditions for deformation of amorphous polymer glasses.

[63] F. Guiu and P. L. Pratt, Stress relaxation and the plastic deformation of solids, Phys. Status Solidi B **6**, 111 (1964).

[64] J. J. Moré, The Levenberg-Marquardt algorithm: Implementation and theory, in *Numerical Analysis: Proceedings of the Biennial Conference Held at Dundee, June 28–July 1, 1977* (Springer, Berlin, Germany, 2006), pp. 105–116.

[65] M. L. Falk and J. S. Langer, Dynamics of viscoplastic deformation in amorphous solids.

[66] A. Haselbacher, On impedance in shock-refraction problems, Shock Waves **22**, 381 (2012).

[67] B. Xu and T. C. O'Connor, Plotted data are freely available at https://github.com/OConnor-Lab/Xu_PRM_2026.